

Relationship among Welding Defects with Convection and Material Flow Dynamic Considering Principal Forces in Plasma Arc Welding

Nguyen Huu Loc^{1,2}, Anh Van Nguyen^{3,4,*}, Han Le Duy⁵, Thanh-Hai Nguyen^{1,2}, Shinichi

Tashiro^{3,*}, Manabu Tanaka³

¹Faculty of Mechanical Engineering, Ho Chi Minh City University of Technology (HCMUT), 268 Ly Thuong Kiet Street, District 10, Ho Chi Minh City 700000, Vietnam

²Viet Nam National University Ho Chi Minh City, Linh Trung Ward, Thu Duc District, Ho Chi Minh City 700000, Vietnam

³Joining and Welding Research Institute, Osaka University, Osaka, Japan

⁴Murata Welding Laboratory, Osaka 532-0012, Japan

⁵Hanoi University of Science and Technology, Hanoi 100-000, Vietnam

Corresponding authors

Anh Van Nguyen

nguyenvananhbkhn@gmail.com

Shinichi Tashiro

tashiro@jwri.osaka-u.ac.jp

Abstract

The material flow dynamic and velocity distribution on the melted domain surface play a crucial role on the joint quality and formation of welding defects. In this study, authors investigated the effects of the low and high currents of plasma arc welding on the material flow and thermodynamics of molten pool and its relationship to the welding defects. The high-speed video camera (HSVC) was used to observe the convection of the melted domain and welded-joint appearance. Furthermore, to consider the Marangoni force activation, the temperature on the melted domain was measured by a thermal HSVC. The results revealed that the velocity distribution on the weld surface was higher than that inside the molten weld pool due to the difference of the massive density between the air and the steel. Moreover, in the case of low welding current (80A) the convection speed of molten was faster than that of the high welding current case (160A) owing to the difference of main driving forces direction and strength, which leading to undercut and humping defects on the weld surface and excessive convex (burn-through) defect at the bottom weld side, respectively. The medium welding current (120A) had two convection patterns with the main flow in backward direction, which resulted in better welding quality without defect. The interaction between the shear force and Marangoni force played a solid state on the convection and heat transportation processes in the plasma arc welding process.

Keywords: Plasma arc welding, thermodynamic, material flow, velocity distribution, welding current

1. Introduction

The thermodynamic of the molten material flow at the melted domain in additive manufacturing (AM) and welding processes plays a principal role on the joint-quality and the appearance of defects such as porosity [1], pore [2], undercut [3], humping [4], spatter [5]. Recently, observation technologies have contributed significantly to clarify the behavior of the material flow in both welding processes and metal AM. Using high speed cameras and innovative X-ray radiography image systems, the convection at the melted domain was estimated in laser welding [6,7] and the friction stir welding process [8]. In another way, using X-ray synchrotron observation systems with a high energy beamline, the keyhole behavior, porosity and fluid flow dynamic were employed in metal AM processes in the UK [9,10], the US [11,12] and Japan [13,14].

Plasma arc welding (PAW) is one advanced joining technology with superior characteristics such as: high current density, constricted arc plasma, and high plasma jet velocity. In PAW, the interaction among plasma arc pressure, plasma gas flow, material flow behavior with the metallurgy phenomena, microstructure formation, and joint quality is very complex. The physical nature behind these processes are inadequately understood owing to the complex material flow thermodynamics that occurs in very short time and extreme conditions.

In relation between the material flow process and joint quality, some papers were addressed for steel and aluminum. Anh et al. [15] reported the effect of the pilot gas component on the behavior of convection flow in the case of SUS 304 material. The result showed that in the case of pilot gas (Ar gas) mixtured with 10% He, the heat input density is much increased and the weld bead becomes wider in comparison to pure Ar case, especially on the top side. In another paper, Nguyen et al., [16] observed the material flow

and keyhole formation at the same time. The results showed that at the cutting arc period the keyhole boundary is changed much especially in longitudinal-section. With support of innovative X-ray image technology, Wu et al. [17] have found out that the dominant forces of material flow behavior in PAW was the arc pressure and shear force. Among them, the arc pressure principally contributes to the formation of the keyhole and the shear force corresponds to the formation of the weld pool. Bin el at. [18] was experimental with aluminum and indicated the difference between the material flow in the cases of steel and aluminum. The results showed that the velocity was much lower in the case of aluminum due to its low mass density. In a recent paper, Manh et al. [19] verified by the experiment that the fluid dynamic of the weld pool in PAW was controlled mainly by shear force. This is totally different to the Tungsten inert gas (TIG) welding process in which the molten flow was mainly controlled by Marangoni force.

However, due to the difficulty of measurement of the material flow of melted domains at high temperature and extreme brightness, the investigations progressed slowly. To overcome this trouble, another approach using calculated tools through numerical simulation has been performed as an efficient alternative method to explode this behavior, furthermore for controlling efficiently this welding process. Rubinsky et al. have utilized a two-dimensional model [20] and a three-dimensional model [21] thermodynamic and material flow for the melted zone. The results display the correlation between the velocity and temperature in vertical cross-sections and horizontal cross-sections of melted domain according to the alteration of welding speed. Wu's team developed a two-dimensional model [22] and a three-dimensional model [23] considering the coupled plasma arc—keyhole—weld pool interactions for calculating the heat transportation and material flow dynamic inside the molten pool. Predicted results show two main convections inside the

melted domain including (1) one outwards eddy along the top surface and another one downwards eddy along the keyhole wall. Recently, Pan et al. [24] predicted the material flow of the molten zone in stationary welding condition (no movement of torch or workpiece). They indicated that two eddies are formed inside the melted domain. This fluid flow dynamic is controlled by four driving forces as explained in [25].

In view of the foregoing discussions on publications, it is apparent that predictions on the fluid flow thermodynamic considering the interaction with the melted domain and keyhole contour have been made, however a whole picture of the relationship among plasma arc – keyhole formation - the behavior of material flow and joint quality has not been clarified yet. For in-deep understanding the behavior of the material flow at the melted domain, a series of investigations of influence of welding parameters have been carried out.

At the first step, authors have adopted the effect of plasma gas flow rate [15] on the eddy formation and the relationship between them to welding defects. In another paper, we discussed the dynamic of material flow inside the melted domain with the change of welding current [26]. In this case, only the material flow inside the weld pool is considered. However, the material flow of the melted domain consisted not only inside the melted domain but also on its surfaces. In other words, those papers lacked the consideration of the convection flow on the melted domain surfaces and of the driving force influence on the convection. Therefore, this investigation is adopted to elucidate the material flow dynamic, velocity, and temperature on the surface of the melted domain. Furthermore, an essential discussion on welding defect formation and dominant forces activation was exploded.

2. Experimental method

Fig.1 presents an experimental setup for this investigation. The welding equipment was included: plasma welding machine NW-300ASR made by Nippon Steel Company and a plasma torch with maximal welding current 300 A. A high-speed video camera (HSVC) was perpendicular with welding seam at an angle 45^0 with workpiece surface to take photographs of the melted domain surface. The back gas was controlled by a small box to cover the lower side of the melted domain without the negative influence from the environment.

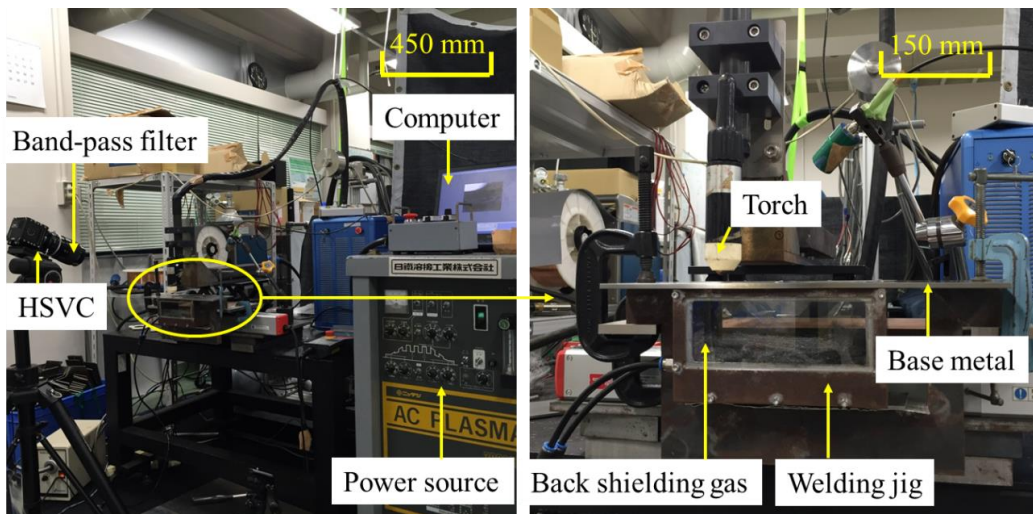


Fig 1. Photograph of experimental setup.

A diagram of experimental setup is described in **Fig. 2**. In this investigation, the main current is changed at three levels: DC 80, 120 or 160 A. The setback for the tungsten electrode was 3 mm. Tungsten electrode diameter was 2.4 mm. Plasma nozzle was 2.0 mm. The arc length was fixed at 5 mm. The workpiece was SUS304 plates with a 4 mm thickness. The torch travel speed was 3 mm s^{-1} . The torch shielding gas, the back gas and the pilot gas were pure Ar with 7.5 l min^{-1} and 5.0 l min^{-1} , 1.7 l min^{-1} respectively.

In order to estimate the convection, tracer particles (zirconia) with a diameter of 0.03 mm

was used. Based on the trajectory and position of particles, the fluid dynamics (convection, material flow and flow velocity) of the melted domain can be elucidated through Dipp-motion software (Detect Co., Ltd). For doing the experiments, holes on the workpiece surfaces were created and zirconia tracers were pushed into before welding. Three holes in a straight-line were made along the welding seam. And then 5 zirconia seeds were pushed in each hole. However, in the case of 160 A, because the size of the weld pool surface is large and long, with a HSVC setting position, it is impossible to visualize the whole melted domain. In order to overcome this difficulty, the zirconia tracers were fed to the melt pool surface by two ways: around the keyhole before welding through the holes on the workpiece surfaces (as indicated above) and at the middle part of the molten pool during welding by a supply device. Details for this supply technique can be seen in our recent paper [27].

Fig. 3 indicates a typical image of this visualization. In this case, because the intensity of the arc plasma is too high, the movement of particles around the keyhole is difficult to visualize clearly. In order to overcome this problem, a diode laser apparatus with the power of 30 W and the wavelength of 940 nm was utilized [19]. The laser head was adapted to cut mostly the brightness of the arc plasma. As a result, the whole melted domain surface can be seen clearly.

In order to discuss the influence of driving forces on the convection and the heat transport, a temperature measurement on the melted domain surface was performed. A schematic can be found out in **Fig 4**. In this case, a Phantom V4 thermal camera was utilized. The measurement mechanism is based on two-color pyrometry [19]. The frame rate was 2000 pfs. The camera had a perpendicular to weld seam. Due to the high brightness of the arc during welding, the temperature on the melted domain surface is impossible to measure

accurately. In order to overcome this issue, the measurement was taken into a period switch off (about 0.01 ms after arc disappearance). It was confirmed by experiment that the decrease of temperature was very slight. And then, this change can be ignored and the result can be utilized to explain the visualization data in this paper. More details for this measurement can be read in ref [19].

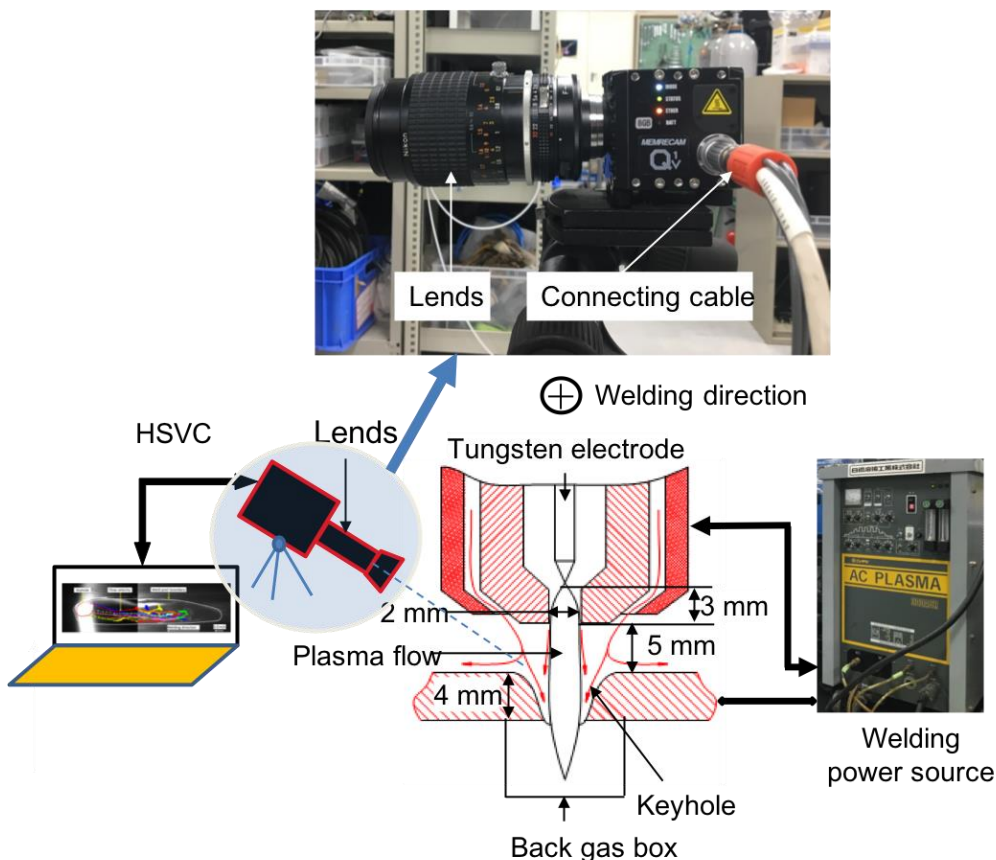


Fig 2 A diagram of experimental setup for observing material flow on the melted domain surface.

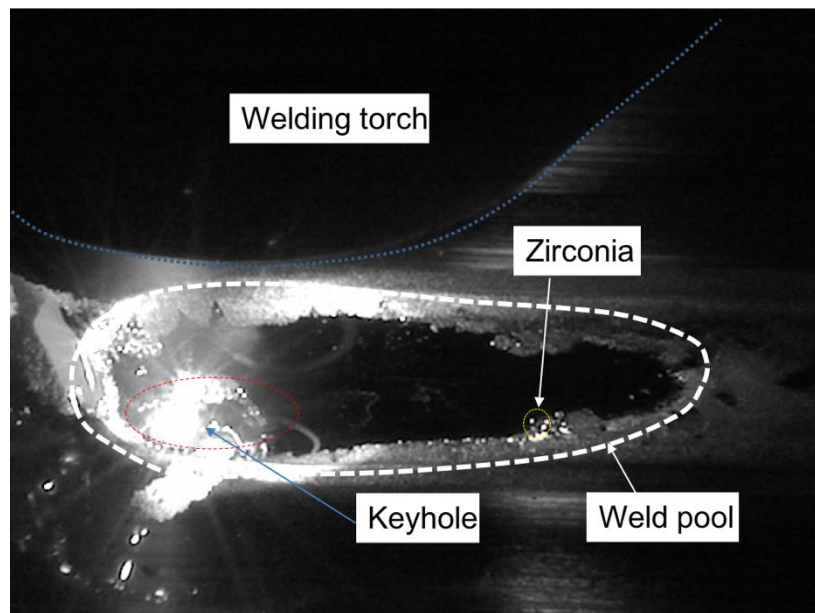


Fig. 3 An example of observation of weld pool and molten material flow.

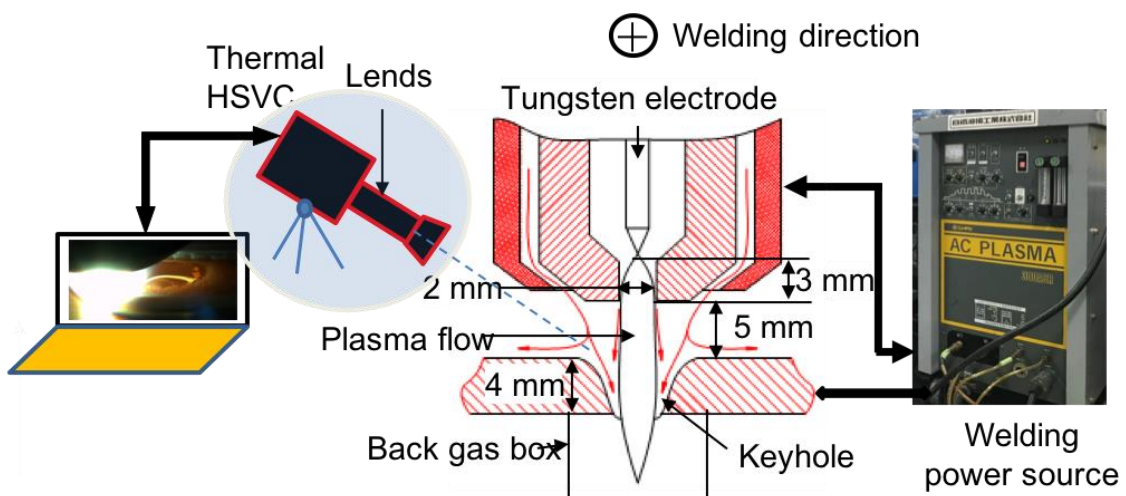


Fig 4. Diagram of temperature measurement on the melted domain surface.

3. Results and discussion

3.1 Welding bead formation and welding defects

Fig. 5 (a), (b) and (c) displayed part of macrostructure of weld bead when welding current is changed at three levels: 80 A, 120 A and 160 A. It can be seen that a clear change of weld bead when current altered from 80 A to 160 A. Weld bead width on the upper part is increased when current varied, especially when current changed from 120 A to 160 A. Weld bead width on the lower part is also much increased when current increases, especially when current increases from 120 A to 160 A. It can be seen that half of total weld seam in the case of 80 A was without melting on the lower side (blind keyhole status).

It was measured to confirm that the weld bead on the top side is about 5.0 mm, 6.3 mm and 7.2 mm in cases of 80 A, 120 A and 160 A respectively. The weld bead on the bottom side is about 1.8 mm, 2.7 mm and 6.1 mm in cases of 80 A, 120 A and 160 A respectively.

Meanwhile, there are almost no welding defects in the case of 120 A. In this case, the keyhole size is larger than that in the case of 80 A, but it is much smaller than that in the case of 160 A, especially on the lower side. In the case of low welding current (80 A), serious humping and deep undercut at both sides can be seen on the upper side. In addition, it seems that there is not good wettability and the weld bead is unstable on the lower side. In the case of 160 A, the weld bead is very wide, especially on the bottom surface. The melted domain seems to sink to the lower side to make a concave on the upper side. On the lower side, a very large bead width can be seen. It can also be seen as the serious excessive convex (burn through) and convex on the lower side.

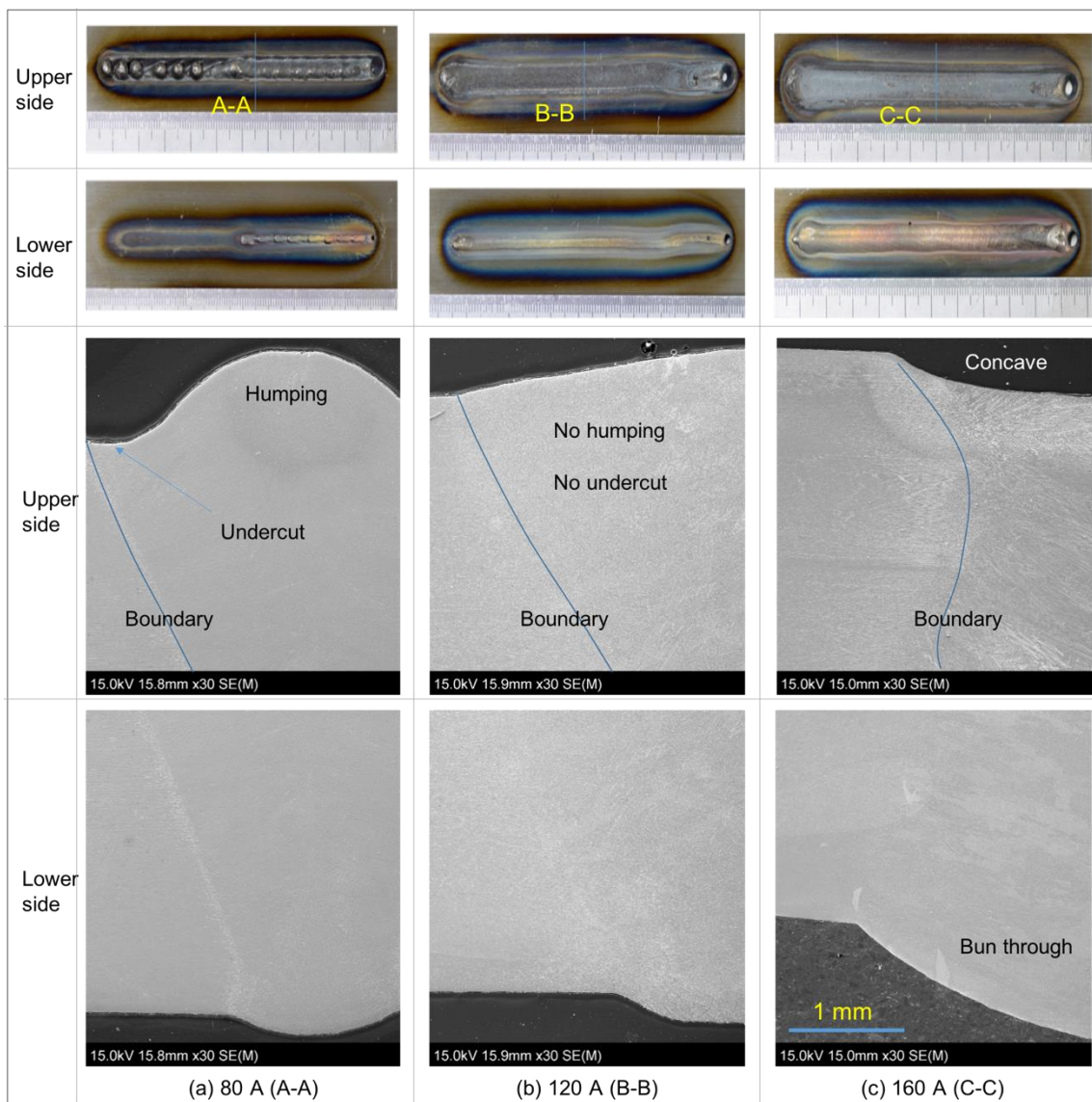


Fig 5 A part of cross-section of weld bead and welding defects.

3.2 Temperature on the melted domain surface

The temperature field on the melted domain surface is presented in **Fig 6**. In the case of 80 A, the highest temperature zone appeared at $X = 5.5 \sim 6.0$ mm. From this position toward the keyhole and toward the ending part of the weld pool, the temperature decreased gradually.

In the case of 120 A, the highest temperature zone is presented at $X = 4.5 \sim 5.5$ mm. Similarly, with the case of 80 A, the temperature decreased gradually toward the keyhole and the rear part of the melted domain.

In the case of 160 A, the highest temperature position is located at $X = 2.0 \sim 2.5$ mm. The temperature slightly reduced from this location toward the keyhole. On the other hand, the temperature was slightly decreased from $X = 2.5$ mm until $X = 7.0$ mm. Afterward, the temperature decreased more sharply from $X = 7.0$ mm toward the rear part of the weld pool.

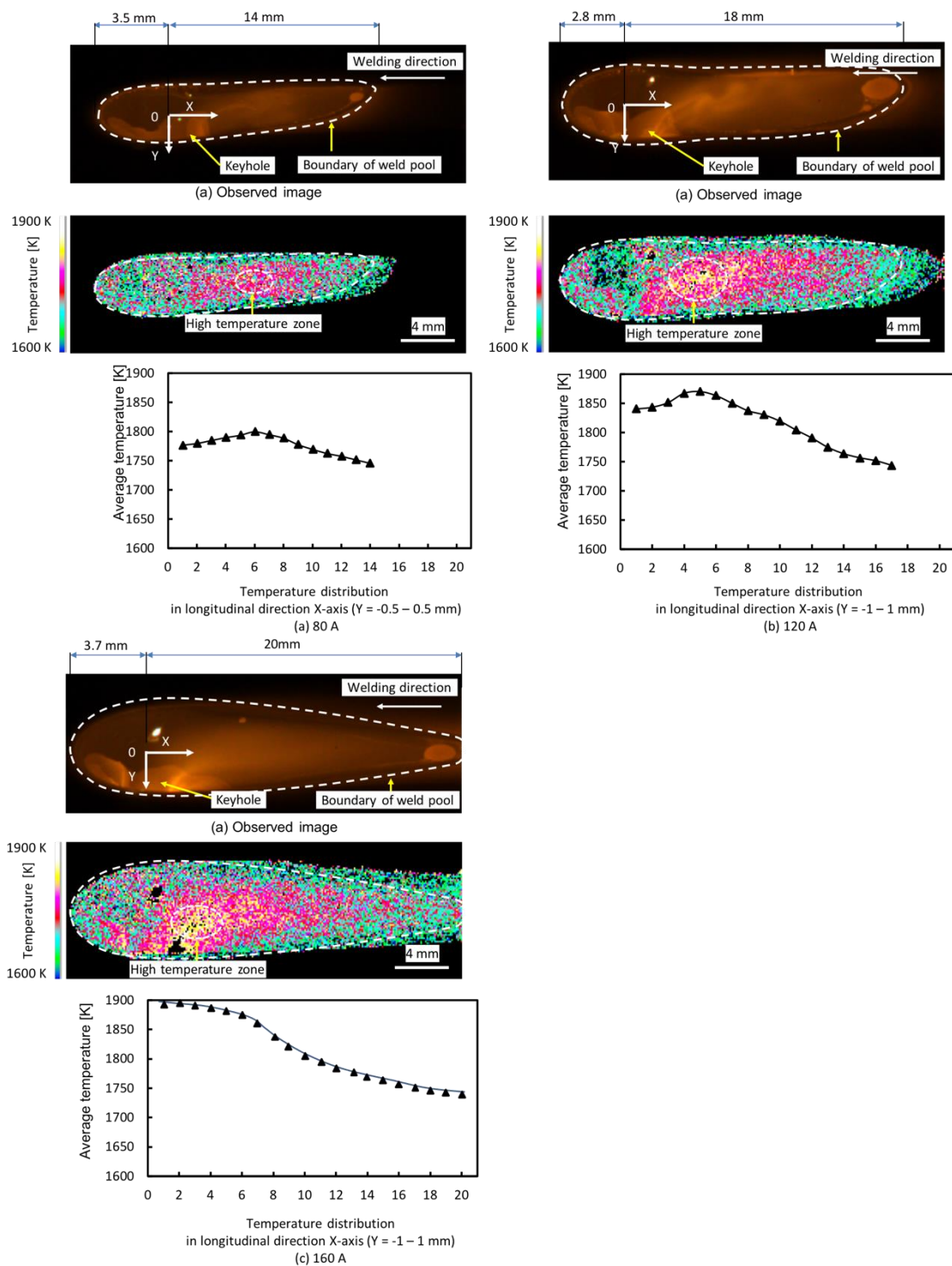


Fig 6. Temperature field on the melted domain surface.

3.3 Material flow dynamic on molten pool surface

Fluid flow dynamics on the top side of the melted domain are described in **Fig. 7** (a), (b)

and (c) corresponding to 80 A, 120 A and 160 A respectively. In this investigation, the

X-axis coincides with the travel line of the torch and Y-axis is perpendicular to that.

In the case of 80 A, particles are moved from the front part of the keyhole toward the rear

part of the keyhole. All particles are strongly accelerated in upward direction from inside

the keyhole center toward the top surface behind the keyhole and are continuously moved

in backward tendency with gradually decreasing velocity before stopping at the ending

region of the melted domain. Most particles are focused on straightly transporting to the

rear part of the melted domain. Near the centerline of the melted domain, the velocity of

particles is much stronger than that at the sides of the keyhole and melted domain.

In the case of 120 A, it is clearly seen that zirconia particles have an initial slow velocity

toward the behind region of the keyhole. From the behind region of the keyhole, there are

two ways for particle movement. Several particles near the center line are moved in

inward tendency and downward tendency just behind the keyhole to the bottom surface.

Several other particles nearby the keyhole sides are accelerated in upward tendency and

are moved to the ending region of the melted domain.

In the case of 160 A, there are two places for putting tracer particles, including in front of

the keyhole and around the middle region of the melted domain as explained above. For

particles round the keyhole, similar to cases of 80 A and 120 A, it starts to move from the

front part of the keyhole. There is only one convective pattern around the keyhole and

two convective patterns around the middle region of the molten pool. For mostly particles around

the keyhole, they run in a downward tendency with a high velocity. However, particles

put on the weld pool from particle supply system near the middle part of weld pool are

moved in two ways: (1) backward and outward tendencies toward the end part of weld pool and (2) forward and outward tendencies toward the keyhole before entering the keyhole center. In addition, several other particles around the keyhole moved in outward tendency at the front part of the keyhole before moving at inward tendency and downward tendency at the rear part of the keyhole.

The weld pool length was about 14 mm, 16 mm and 23 mm in the cases of 80 A, 120 A, and 160 A respectively. Meanwhile, its width was about 5.0 mm, 6.2 mm and 7.1 mm in the cases of 80 A, 120 A, and 160 A respectively. From this photograph it can be seen the undercut in the case of 80 A, and concave on top surface in the case of 160 A.

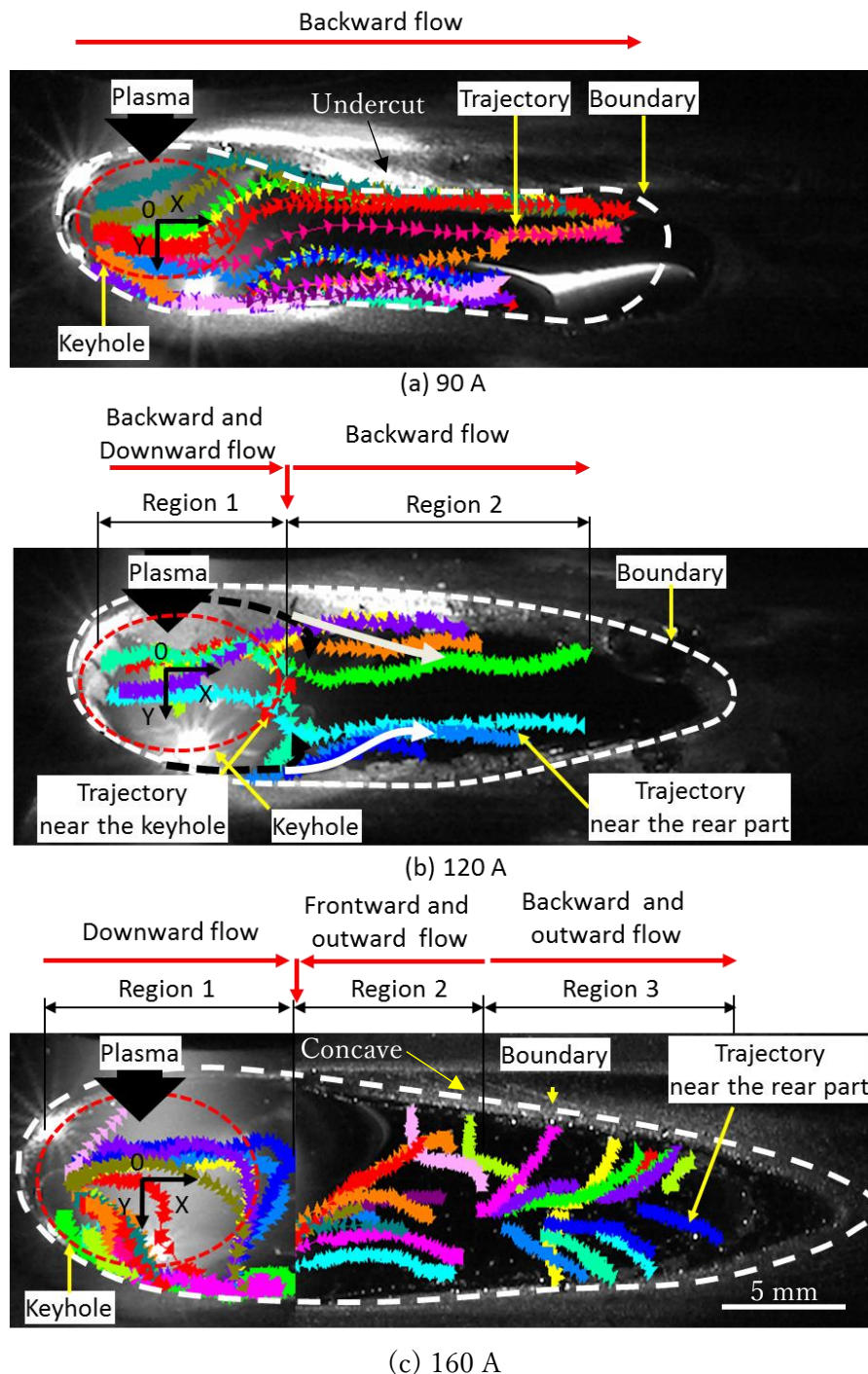


Fig 7 Material flow dynamic on the melted domain surface.

3.4 Velocity of material flow on the melted domain surface

In this subsection, the flow velocity is analyzed in detail. In order to discuss the velocity distribution on the melted domain surfaces, the velocity is considered at several longitudinal-sections along X-axis.

The melted pool width is largest in the case of 160 A, and smallest in the case of 80 A. As a result, the number of longitudinal-sections are different in all cases. They are 6 longitudinal-sections (160 A), 5 longitudinal-sections (120 A), and 4 longitudinal-sections (80 A). On the other hands, due to the very long weld pool in the case of 160 A, the velocity graph was divided two domains according to the HSVC setting position change. One of them is around keyhole zone, and another one is from the middle part until the ending part of the weld pool.

The flow velocity field on the upper side around the keyhole in the case of 160 A is described in **Fig. 8**. The velocity increased before it gradually decreased. However, at only $Y = -3 \sim -1$ mm, the velocity decreased from $X = 2$ until $X = 6$ mm. In other cases, the velocity of molten material flow generally increased firstly, before it decreased from $X = 5.0 \sim 6.0$ mm. For the backward convection pattern, the maximal velocity was about 0.98 ms^{-1} at $X = 0.0$ mm. Meanwhile the maximal velocity of downward convection pattern was about 1.12 ms^{-1} at $X = 5.5$ mm.

Distribution of flow velocity around the ending part ($X = 7.0 \sim 23.0$ mm) in the case of 160 A is shown in **Fig. 9**. The velocity increased from the ending part of the melted domain toward the keyhole, especially around $X = 7 \sim 8$ mm. At $X = 7$ mm, the velocity was very high. This is caused by the inward flow from the ending part of the weld pool until the keyhole and in downward flow from the upper side toward the lower side of the melted region. At $Y = -3.0 \sim -2.0$ mm region, the velocity is mostly unchanged along the

weld pool surface. This case be explained because the tracer particle was detected just within $X = 12 \sim 16.5$ mm. In this area, the forward movement of tracer particles is stable with low velocity. The maximal velocity was about 1.2 ms^{-1} at $X = 8.0$ mm in the case of $Y = 1.0 \sim 2.0$ mm. The minimal velocity was about 0.15 ms^{-1} at $X = 18.8$ mm in the case of $Y = -1.0 \sim 0.0$ mm.

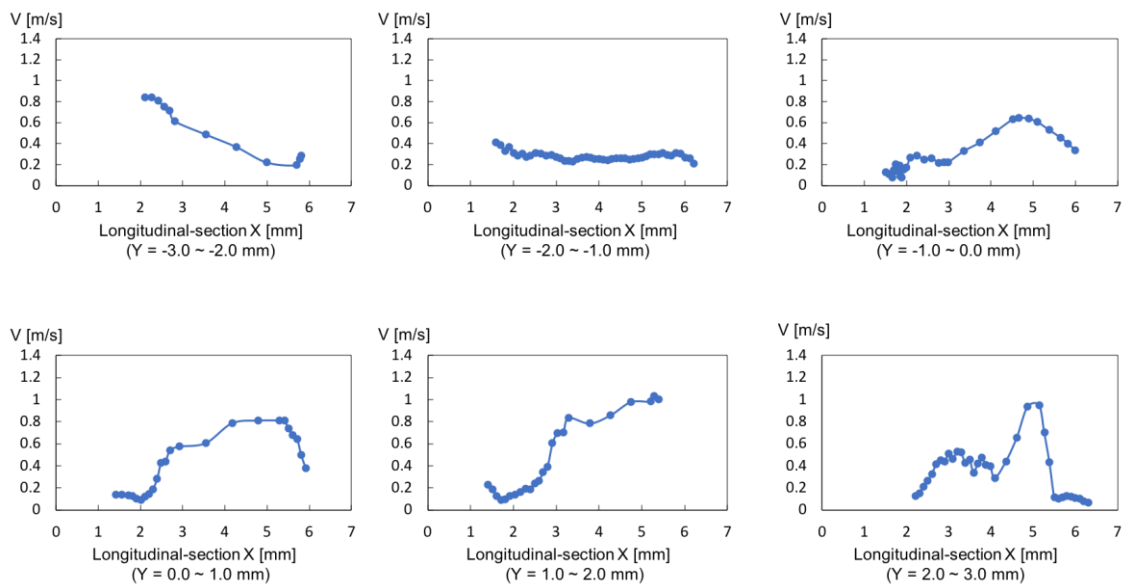


Fig 8 Flow velocity graph around keyhole in the case of 160 A.

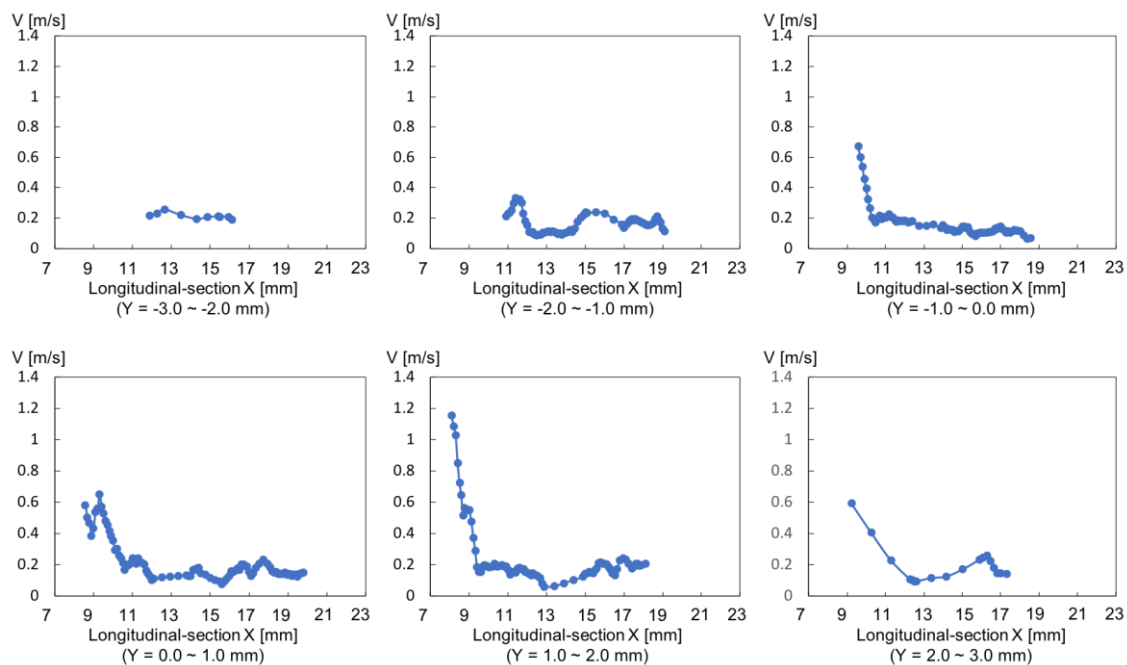


Fig 9 Flow velocity graph around ending part in the case of 160 A.

The velocity distribution on the upper side in the case of 120 A is exhibited in **Fig. 10**. In this case, the velocity increased from $X = 0.0 \sim 6.0$ mm, and then decreased from $X = 6.0$ until the ending part of the weld pool ($X = 15$ mm). As indicated in **Fig. 7**, there are two convective patterns in the case of 120 A. As a result, it can be considered that the convection flow around the keyhole in inward-backward-downward directions matched with the increased velocity area ($X = 2.0 \sim 6.0$ mm). And the convection flow from the middle part until the ending part of the melted domain corresponded to the decreased velocity area from $X = 6.0 \sim 15.0$ mm. The maximal velocity was about 0.89 ms^{-1} at $X = 6.0$ mm in the case of $Y = 0.0 \sim 1.0$ mm. The velocity at the ending part of the weld pool was about 0.19 ms^{-1} at $X = 14.5$ mm.

The velocity in the case of 80 A is described in **Fig. 11**. In this case, the velocity increased sharply from $X = 2.0$ mm until $X = 6.0$ mm. And then the velocity rapidly decreased with $X = 6.0 \sim 8.0$ mm. After that, the velocity moderately deducted until the ending part of the melted region. The velocity reached the maximal value of 1.4 ms^{-1} at $X = 6.0$ mm in

the case of $Y = 1.0 \sim 2.0$ mm. The velocity was about 0.15 ms^{-1} at the keyhole wall. The velocity at the ending part of the molten pool was 0.25 ms^{-1} at $X = 11.7$ mm in the case of $Y = 1.0 \sim 2.0$ mm.

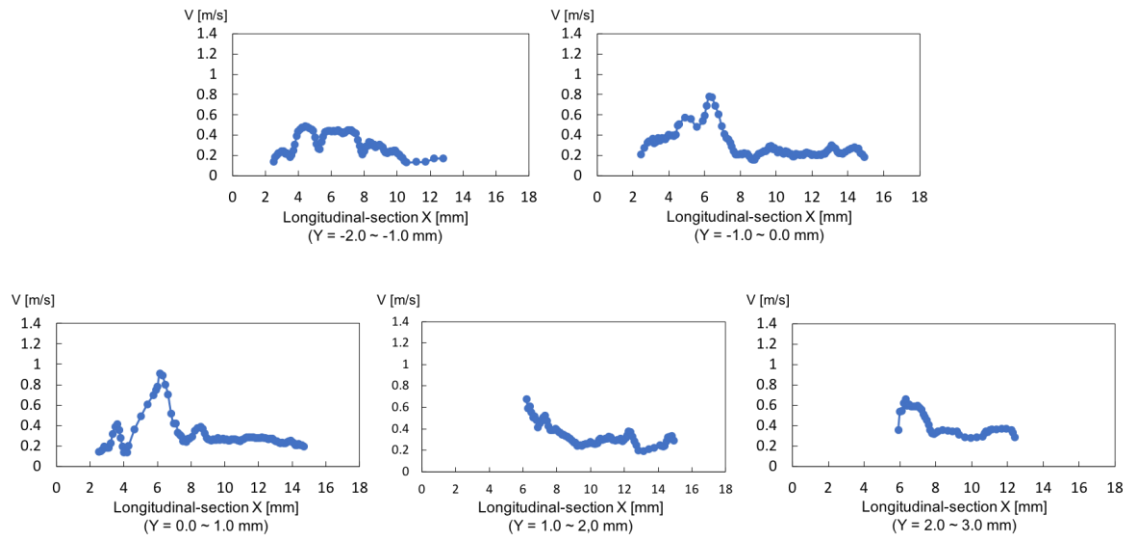


Fig 10 Flow velocity graph in the case of 120 A.

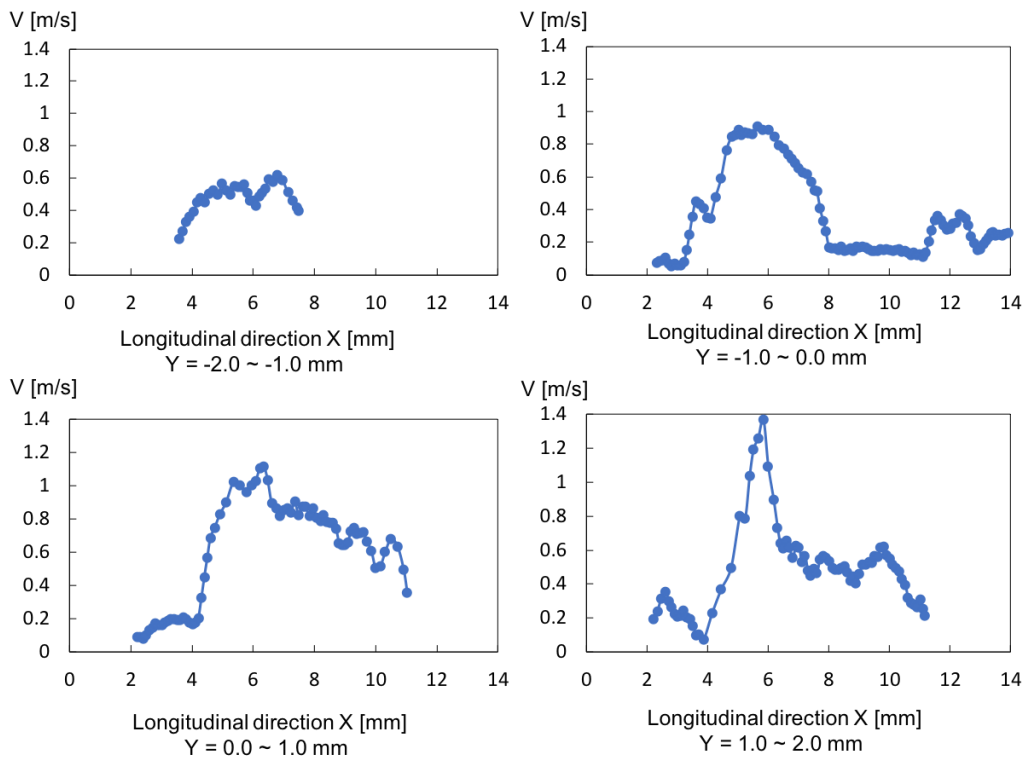


Fig 11 Flow velocity graph in the case of 80 A.

3.5 Discussion

To consider the relationship among welding defects with convection and material flow dynamic, a deep discussion can be opened as follows.

In the case of 80 A, the particles directly moved with high velocity toward the ending region of the melted domain.

Meanwhile, in the case of 120 A, the particles behind the keyhole were with two movement trends including: backward and downward directions around the weld pool centre (particles at weld pool centre) and backwards toward the ending region of the melted domain (particles at side weld pool). Furthermore, in this case, the velocity is less than that in comparison to the case 80 A.

In the case of 160 A, the particles at the behind half part of the weld pool moved with trends in outward and backward directions toward the side weld pool, rather than transported directly to the rear part of the melted domain. Meanwhile the particles at the front half part of the weld pool tend to move in frontward and downward directions. On the other hand, particles around the keyhole are transported with downward direction along the keyhole wall. In this case, the velocity was higher than that in the case of 120 A but it was lower than that in the case of 80 A.

On the other hand, as aforementioned above, because of very low heat input in the case 80 A, at first the blind keyhole status is formed within the front half part of the welding seam (see **Fig 5 (a)**). During this period, the heat input is grown rapidly due to heat transfer from the torch toward the keyhole, weld pool in downward direction to form the opening keyhole status at the behind half part of the weld seam (see **Fig 5 (a)**). However, this status is unstable and the weld bead on the lower side was unstabilized. On the other

hand, in a recent publication, it was discussed that in the case of small keyhole diameter (low welding current), the plasma flow was mainly in reverse direction from the middle region of the keyhole toward the upper side of the melted domain [26]. In other papers, it was analyzed that plasma flow and arc pressure were the dominant driving forces for the convection and heat transportation in the PAW process, rather than Marangoni force [19, 31]. This means that the heat is dominantly transported in upward direction with high speed under the control of plasma flow and arc pressure. From these results, it can be considered that the deep undercut and serious humping phenomena on the top surface as seen in **Fig 5 (a)** and **Fig 7 (a)** in the case of 80 A was mainly related to the high velocity and straight movement of particles toward the ending part of the melted domain with same mechanism in refs [28, 29].

When current is 120 A, the increased heat input is supported to the melted domain in order to create an opening keyhole status immediately after starting the arc. In this case, the plasma flow and the arc pressure are allocated in both directions: upwards along the top side and downwards alongside the keyhole wall [26]. The balance of the heat input on both the lower side and the upper side is suitable to procedure a weld seam with no undercut and humping defects on the top surface and no excessive convex (burn-through) on the bottom surface (see **Fig 5 (b)**).

In the case of high welding current (160 A), the heat input under influence of the arc pressure and the plasma flow on the keyhole profile (very large diameter and small wall inclination) was much increased, a very large pool volume and a wide keyhole contour as can be seen in **Fig. 5 (c)** and **Fig. 7 (c)** [14]. The plasma flow and the arc pressure were

almost pushed down. The heat input was concentrated mainly on the lower surface. This formed a very wide weld bead and an enormous weldment volume (excessive convex) especially on the lower side. In addition, in a recent paper [26], authors discussed about the molten material flow behaviour inside the melted domain, the results showed that the material flow inside the melted domain is diverted at $X = 3.5 \sim 4.5$ mm in the case of 160 A (from upwards to frontwards), at $X = 5.0 \sim 6.0$ mm in the case of 120 A (from backwards to downwards) and at $X = 6.0 \sim 7.0$ mm in the case of 80 A (from backwards to downwards). On the other hand, authors have also measured the flow velocity inside the weld pool. The maximal velocity was about 0.34 ms^{-1} in the case of 160 A. This maximal velocity occurs at the keyhole bottom surface (nearby keyhole). Meanwhile, the maximal velocity was 0.40 ms^{-1} occurring at the keyhole top surface in the case of 80 A (nearby keyhole). This change (velocity was increased when the current was low and in contrast) had similar tendency with the velocity change on the melted domain surface in this paper, in which the velocity in the case of 160 A was lower than the case of 80 A, but was higher than the case of 120 A. Furthermore, from ref [26] and the results in this paper it can be considered that maximal velocity values inside the melted domain were lower in comparison to the maximal velocity on the melted domain surface at the same region. This difference can be explained based on the difference of massive density between the steel and air. It has been known well that the massive density of steel is much higher than the air. This can affect the movement of particles when they are put inside. In the case of welding steel plates, a melted zone is created. When a tracer particle is pushed inside this zone, it is more difficult to move in comparison to the case the particle is pushed on the surface of this zone (in which half part of the particle belongs to this zone and another half part belongs to the air). Meanwhile, the convection pattern tended to outward and

backward directions at the behind half part in the case of high welding current (160 A) caused a very large and long weld pool. Furthermore, the convection flow in downward direction around the keyhole resulted in a large heat input amount pushing down to the bottom surface [30]. This is directly related to the excessive convex phenomenon on the lower side and the concave on the upper side of the melted domain.

In order to explain the behavior of material flow and convection patterns under the activity of driving forces, an underlying consideration is performed.

As found out in recent papers [19, 27] the driving forces in PAW process are shear force (plasma flow and arc pressure) and Marangoni force. Meanwhile, the buoyancy force and electromagnetic force are not large enough to control the material flow and convection patterns in the PAW process. The shear force is created by two components: upward direction at the upper side of the melted domain and downward direction alongside the keyhole.

In the case of low welding current (80 A), the highest temperature zone was located at the weld pool centre alongside from the keyhole centre about 5.5 mm (at $X = 5.5$ mm). In this case if considering only Marangoni force influence, the convection flows must be from the high temperature zone toward the low temperature zone. In other words, the material flow must be from the weld pool centre toward the weld pool side, the keyhole and the rear part of the weld pool. However, as seen in **Fig 7 (a)**, the fluid flows were mostly transported in backward direction from the keyhole. Furthermore, the shear force in this case was mostly in upward and backward directions as explained above and ref [26]. It means that the shear force component in upward direction was stronger than the Marangoni force. The convection flow was controlled mainly by a strong shear force and

the Marangoni force in opposite directions. In this case, shear force is the main dominant force.

In the case of 120 A, a similar situation with the above case can be seen. The highest temperature zone was at $X = 4.5$ mm. Under the activity of the Marangoni force, the convection flow should be from this zone toward the side, the keyhole and the rear part of the weld pool (high temperature toward low temperature). However, from **Fig 7 (b)** it can be seen that one convection flow was downward around the keyhole, and another one was transferred straight to the rear part of the weld pool. It means that around the keyhole, the convection flow is controlled by a weak shear force component and a Marangoni force in opposite directions. As a result, the material flow was in a downward direction. In this case, the Marangoni force is the main dominant force. For the convection flow toward the rear part of the weld pool, the shear force and Marangoni force are the same direction in backward direction. Furthermore, the shear force component in upward direction was weaker in comparison to the case of 80 A, so the particle velocity was smaller.

In the case of 160 A, the keyhole size becomes very large and more straight from top side toward bottom side. As a result, the share force component in downward direction was much stronger than the share force component in upward direction [26]. On the other hand, the highest temperature zone was at around $X = 2.5$ mm. Furthermore, the temperature slightly decreased from $X = 2.5$ mm until $X = 6.0$ mm. After that the temperature decreased more sharply from $X = 6.5$ mm until the rear part of the weld pool. In this case, under the activity of Marangoni force, the convection flow should be in frontward direction toward the keyhole, backward direction toward the end part of the weld pool and outward direction to the side of the weld pool from the high temperature

zone. However, as seen in **Fig 7 (c)**, the convection flow was in frontward at region 1, frontward in region 2 and backward in region 3. So, in this case, the convection flow around the keyhole is controlled by a very strong shear force component in downward direction and frontward direction Marangoni force. The convection flow in frontward direction in region 2 was controlled by a very weak Marangoni force (due to the slight change of temperature at this region) in backward direction and a strong shear force component in downward direction. And the convection flow in backward direction at region 3 was controlled mainly by Marangoni force in backward direction and very weak shear force component in backward direction. Furthermore, due to the very strong shear force component in the downward direction around the keyhole, the tracer particle's velocity was much higher than that in the case of 120 A.

Summary, the shear force due to the plasma flow and arc pressure was changed depending on the keyhole contour. And then, the share force components in upward or downward directions become stronger or weaker. The Marangoni force was changed with the variation of the temperature distribution. It becomes stronger when the temperature is reduced largely and in contrast it becomes weaker when the temperature is reduced slightly in the same distance scale. The interaction between shear force and the Marangoni force principally controlled the convection patterns change in PAW process.

4. Conclusion

In this paper, weld beads, material flow, velocity and temperature on melted domain surface in relation to welding defects were discussed in detail. Several main conclusions can be seen:

1. No welding defects were seen in the case of 120 A but serious humping and undercut phenomena was observed in the case of 80 A. Meanwhile, concave and burn-through occurred in the case of 160 A.
2. A detailed analysis of convection and flow velocity on the melted domain surface in PAW was performed to determine the relationship to the welding defects formation.
3. The welding defects (undercut and humping) related to a high-speed fluid flow on the surface of the melted domain in the case of 80 A.
4. The excessive convex (burn-through) on the bottom surface was with a reverse fluid flow in downward direction around the keyhole in the case of 160 A.
5. The convection speed was faster in the case of low welding current (80 A). Meanwhile, the slower speed occurred in the case of high welding current (160 A).
6. The measured results were compared with the convection inside the weld pool. In this case, the maximal velocity on the surface was higher than inside the molten pool due to the difference of the massive density between the air and the steel.
7. The temperature distribution difference on the melted domain surface caused the Marangoni force.
8. The interaction between shear force and Marangoni force mainly controlled the convection and heat transportation in the weld pool.

Acknowledgement

The authors acknowledge Mr. Murata at Murata Welding Laboratory for encouraging to do this work. Authors acknowledge also Mr. Trinh Quang Ngoc from Osaka University for the support during a part of experiments. We would also like to thank HCMUT, VNU-HCM for the support of time and facilities for this work.

Authors contribution

Nguyen Huu Loc: experiment, data analysis, writing-revise; Anh Van Nguyen: conceptualization, methodology, writing-revise, supervision; Han Le Duy: experiment, data analysis, write-revise; Thanh-Hai Nguyen: facilities, discussion; Shinichi Tashiro: supervision, discussion; Manabu Tanaka: supervision, discussion, facilities.

Funding

This investigation was funded by Ho Chi Minh City (HCMUT) under grant number CK-2020-01.

Data availability

Data can be available based on the requirements to verify this work.

Declarations

Ethical approval: No ethical approval was requested for this work

Consent to participate: Not applicable.

Consent for publication: All authors have read and approved the submitted manuscript.

Competing interests: The authors declare no competing interests.

Reference

- 1) Cang Zhao; Niranjan D. Parab; Xuxiao Li; Kamel Fezza; Wenda Tan; Anthony D. Rollett; Tao Sun. Critical instability at moving keyhole tip generates porosity in laser melting. *Science*. 2020, 370, 1080–1086
- 2) Mostafa Yakout; Ian Phillips; M.A. Elbestawi; Quyin Fang. In-situ monitoring and detection of spatter agglomeration and delamination during laser-based powder bed fusion of Invar 36. *Optics & Laser Technology*. 2021, 136, 106741
- 3) R. Zhong; J. Chen; C. S Wu; G. K. Padhy. Influence of molten metal flow on undercutting formation in GMAW. *Sci. Tech. of Welding and Joining*. 2016, 22, 1-10
- 4) T. C. Nguyen; D. C. Weckman; D. A Johnson; H. W. Kerr. The humping phenomenon during high speed gas metal arc welding. *Sci. Tech. of Welding and Jining*. 2005, 10, 447-459
- 5) Yunhui Chen; Samuel J. Clark; Chu Lun Alex Leung; Lorna Sinclair; Sebastian; et.al.. In-situ Synchrotron imaging of keyhole mode multi-layer laser powder bed fusion additive manufacturing. *Applied material today*. 2020, 20, 100650
- 6) Kawahito Yousuke; Nakada Kouki; Uemura Yosuke; Mizutani Masami; Nishimoto Kouji; Kawakami Horoshi; Katayama Seiji. Relationship between melt flows based on three-dimensional X-ray transmission in-situ observation and spatter reduction by angle of incidence and defocusing distance in high-power laser welding of stainless steel. *Quarterly journal of japan welding society*. 2016, 34, 239-248
- 7) Yousuke Kawahito; Hongze Wang. In-situ observation of gap filling in laser butt welding. *Scipta materialia*. 2018, 154, 73-77
- 8) Y. Morisada; H. Fujii; Y. Kawahito; K. Nakata; M. Tanaka. Three-dimensinal visualization of material flow during friction stir welding by two pairs of X-ray

transmission system. *Scripta materialia*. 2011, 65, 1085-1088

9) Lee Aucott; HongBiao Dong; Wajira Mirihange; et al.. Revealing internal flow behaviour in arc welding and additive manufacturing of metals. *Nature communications*. 2018, 9, 5414

10) Yunhui Chen; Samuek J. Clark; Yuze Huang; Lorna Sinclair; et al.. In situ X-ray quantification of melt pool behaviour during directed energy deposition additive manufacturing of stainless steel. *Material Letters*. 2021, 286, 129205

11) Ross Cunningham; Cang Zhao; Niranjan Prab; et al.. Keyhole threshold and morphology in laser melting revealed by ultrahigh-speed x-ray imaging. *Science*. 2019, 363, 849-852

12) Quilin Guo; Cang Zhao; Lianghua Xiong; et al.. In-situ full-field mapping of melt flow dynamics in laser metal additive manufacturing. *Additive manufacturing*. 2019, 31, 100939

13) Masanori Miyagi; Jiye Wang. Keyhole dynamics and morphology visualized by in-situ X-ray imaging in laser melting of austenitic stainless steel. *Journal of Materials Processing Technology*. 2020, 282, 116673

14) Bin Xu; Shujun Chen; Shinichi Tashiro; Fan Jiang; Manabu Tanaka. Physical mechanism of material flow in variable polarity plasma arc keyhole welding revealed by in situ X-ray imaging. *Phys. Fluids*. 2021, 33, 017121

15) Nguyen Van Anh; Shinichi Tashiro; Bui Van Hanh; Manabu Tanaka. Influence of plasma gas on the behavior of convention flow on weld pool surface. *Quarterly journal of the Japan welding society*. 2017, 35, 98s-102s.

16) Nguyen Van Anh; Ngo Huu Manh; Shinichi Tashiro; Manabu Tanaka. Behavior of keyhole exit during the cutting arc period. *Material engineering forum*. 2018, 26, 92-

97.

- 17) Dongsheng Wu; Shinchi Tashiro; Xueming Hua; Manabu Tanaka. A novel electrode-arc-weld pool model for studying the keyhole formation in the keyhole plasma arc welding process. *J. Phys. D: Appl. Phys.* 2019, 52, 165203.
- 18) Bin Xu; Fang Jiang; Shun Chen; Shinchi Tashiro; Nguyen Van Anh; Manabu Tanaka. Material flow analyses of high-efficiency joint process in VPPA keyhole flat welding by X-ray transmission system. *Journal of Cleaner Production.* 2019, 250, 119450.
- 19) Ngo Huu, M.; Nguyen Van, A.; Nguyen Van, T.; Tran Hai, D.; Nguyen Van, T.; Nguyen Tien, D.; Nguyen, T.-H. Material Flow Behavior on Weld Pool Surface in Plasma Arc Welding Process Considering Dominant Driving Forces. *Appl. Sci.* 2020, 10, 3569.
- 20) Y. F. Shu; B. Rubinsky. Two-dimensional heat transfer study on the keyhole plasma arc welding process. *Int. J. Heat mass transfer.* 1988, 31, 1409-1421.
- 21) Russell G. Keanini; Boris Rubinsky. Three-dimensional simulation of the plasma arc welding process. *Int. J. Heat mass transfer.* 1993, 36, 3283-3298.
- 22) Xiaoxia Jian; C. S Wu. Numerical analysis of the coupled arc-weld pool-keyhole behaviors in stationary plasma arc welding. *International journal of heat and mass transfer.* 2015, 84, 839-847.
- 23) Yan Li; Yanhui Feng; Yafei Li; Xinxin Zhang; Chuan Song Wu. Plasma arc and weld pool coupled modeling of transport phenomena in keyhole welding. *International journal of heat and mass transfer.* 2016, 92, 628-638.
- 24) Jiajing Pan; Shengsun Hu; Lijun Yang; Shujin Chen. Numerical analysis of the heat transfer and material flow during keyhole plasma arc welding using a fully coupled tungsten plasma anode model. *Acta materialia.* 2016, 118, 221-229.

25) Manabu Tanaka; J J Lowke. Predictions of weld pool profiles using plasma physics. *Journal of Physics D: Applied Physics*. 2007, 40, R1.

26) Nguyen Van Anh; Shinichi Tashiro; Ngo Huu Manh; Bui Van Hanh; Manabu Tanaka. Effect of the eddies formed inside a weld pool on welding defects during plasma keyhole arc welding. *Journal of manufacturing process*. 2020, 59, 649-657.

27) Nguyen Van Anh; Shinichi Tashiro; Bui Van Hanh; Manabu Tanaka. Experimental investigation of weld pool formation process in plasma keyhole arc welding. *Journal of Physics D: Applied Physics*. 2018, 51, 015204.

28) Peter M. Norman; Jan Karlsson; Alexander F. H. Kaplan. Mechanisms Forming Undercuts during Laser Hybrid Arc Welding. *Physics Procedia*. 2011, 12, 201-207.

29) R Zong; J Chen; C. S Wu; M. A Chen. Undercutting Formation Mechanism in Gas Metal Arc Welding. *Welding journal*. 2016, 95, 174-184.

30) Zeynab Abbasi; Donald Yuhas, Lu Zhang; Alexandra-Del-Carmen Basantes; Niloofar Nabil Tehrani; Didem Ozevin; Ernesto Indacochea. The Detection of Burn-Through Weld Defects Using Noncontact Ultrasonics. *Materials*. 2018, 11, 128.

31) Nguyen Van Anh; DongSeng Wu; Shinichi Tashiro; Manabu Tanaka. Undercut formation mechanism in the keyhole plasma arc welding. *Welding journal*. 2019, 98, 204-212.